

0.003

BetaCoV/Shenzhen/HKU-SZ-005/2020[EPI\_ISL\_405839]  
MN975262\_Wuhan\_seafood\_market\_pneumonia\_virus\_isolate\_2019-nCoV\_HKU-SZ-005b\_2020  
BetaCoV/USA/AZ1/2020[EPI\_ISL\_406223]  
MN974709\_Wuhan\_seafood\_market\_pneumonia\_virus\_isolate\_2019-nCoV/USA-AZ1/2020  
BetaCoV/Shenzhen/HKU-SZ-002/2020[EPI\_ISL\_406030]  
MN983694\_Wuhan\_seafood\_market\_pneumonia\_virus\_isolate\_2019-nCoV\_HKU-SZ-002a\_2020  
BetaCoV/Guangdong/GDF919/2020[EPI\_ISL\_406992]  
BetaCoV/England/01/2020[EPI\_ISL\_407071]  
**BetaCoV/Belgium/GHB-03021/2020**  
BetaCoV/Wuhan/WH04/2020[EPI\_ISL\_406801]  
BetaCoV/USA/WA1/2020[EPI\_ISL\_404895]  
MN985325\_Wuhan\_seafood\_market\_pneumonia\_virus\_isolate\_2019-nCoV/USA-WA1/2020  
MN994467\_Wuhan\_seafood\_market\_pneumonia\_virus\_isolate\_2019-nCoV/USA-CA1/2020  
MN988713\_Wuhan\_seafood\_market\_pneumonia\_virus\_isolate\_2019-nCoV/USA-L1/2020  
BetaCoV/Germany/BavPat1/2020[EPI\_ISL\_406062]  
BetaCoV/Zhejiang/WZ-01/2020[EPI\_ISL\_404227]  
BetaCoV/Wuhan/WIV03/2019[EPI\_ISL\_402127]  
MN995627\_Wuhan\_seafood\_market\_pneumonia\_virus\_isolate\_WIV02  
BetaCoV/Fujian/2020F077/2020[EPI\_ISL\_406534]  
BetaCoV/Finland/1/2020[EPI\_ISL\_407079]  
BetaCoV/Wuhan/WH03/2020[EPI\_ISL\_406800]  
BetaCoV/Wuhan/WH01/2019[EPI\_ISL\_406798]  
MN996528\_Wuhan\_seafood\_market\_pneumonia\_virus\_isolate\_WIV04  
BetaCoV/China/WHU02/2020[EPI\_ISL\_406717]  
BetaCoV/China/WHU01/2020[EPI\_ISL\_406716]  
MN988669\_Wuhan\_seafood\_market\_pneumonia\_virus\_isolate\_2019-nCoV\_WHU02  
MN988668\_Wuhan\_seafood\_market\_pneumonia\_virus\_isolate\_2019-nCoV\_WHU01  
BetaCoV/Singapore/1/2020[EPI\_ISL\_406973]  
BetaCoV/Hangzhou/HZ-1/2020[EPI\_ISL\_406970]  
MN996531\_Wuhan\_seafood\_market\_pneumonia\_virus\_isolate\_WIV07  
MN996530\_Wuhan\_seafood\_market\_pneumonia\_virus\_isolate\_WIV06  
BetaCoV/Norviba/01/2020[EPI\_ISL\_403962]  
MN996529\_Wuhan\_seafood\_market\_pneumonia\_virus\_isolate\_WIV05  
BetaCoV/Wuhan-Hu-1/2019[EPI\_ISL\_402125]  
MN980847\_3\_Wuhan\_seafood\_market\_pneumonia\_virus\_isolate\_Wuhan-Hu-1  
NC\_045122\_2\_Wuhan\_seafood\_market\_pneumonia\_virus\_isolate\_Wuhan-Hu-1  
BetaCoV/Australia/VIC01/2020[EPI\_ISL\_406844]  
BetaCoV/Taiwan/2/2020[EPI\_ISL\_406031]  
BetaCoV/France/DF0372/2020[EPI\_ISL\_406596]  
MN994468\_Wuhan\_seafood\_market\_pneumonia\_virus\_isolate\_2019-nCoV/USA-CA2/2020

SARS-CoV-2 strain BetaCoV/Belgium/GHB-03021/2020 (direct sequencing)  
from nasal swap obtained from traveler returning from Wuhan in early 02/2020

Passage (P) Cell line Trypsin (4 µg/mL) Antibiotics/fungicide	P1 HuH7 yes yes	P2 Vero-E6 yes yes	P3 Vero-E6 no yes	P4 Vero-E6 no yes	P5 Vero-E6 no no	P6 Vero-E6 no no
<i>Exclusion of adventitious agents (clinical microbiology panel)</i>						
Days in culture Cytopathic effect Titer (TCID <sub>50</sub> /mL)	7 50% -	7 80-90% -	5 80-90% -	5 full 3.8x10 <sup>6</sup>	3 full 3.3x10 <sup>4</sup>	3 full 4.8x10 <sup>7</sup>
Sequencing <b>S protein variants</b>					Minion <b>Mixed population</b> 85% WT + 15% 9+5aa del	Minion 100% 9+ 5aa del

50 90

Wuhan-Hu-1 STQDLFLPFFFSNVTWFHAIHVSGTNGTKRFDNPVLPFFNDGV  
GHB-P0 STQDLFLPFFFSNVTWFHAIHVSGTNGTKRFDNPVLPFFNDGV  
GHB-P6 STQDLFLPFFFSNVTWFHA-----KRFDNPVLPFFNDGV  
SARS-CoV-1 (Tor2) LTQDLFLPFYSNVTWFHT-----HTFGNPVLPFFKDI  
\*\*\*\*\* \*\*

658 S1/2

Wuhan-Hu-1 NSYECDIPIGAGICAS<sup>Y</sup>QTQ<sup>T</sup>NS<sup>PR</sup>RR<sup>RS</sup>VSASQSI<sup>I</sup>AYTMS  
GHB-P0 NSYECDIPIGAGICAS<sup>Y</sup>QTQ<sup>T</sup>NS<sup>PR</sup>RR<sup>RS</sup>VSASQSI<sup>I</sup>AYTMS  
GHB-P6 NSYECDIPIGAGICAS<sup>Y</sup>Q-----PR<sup>RR</sup>RR<sup>RS</sup>VSASQSI<sup>I</sup>AYTMS  
SARS-CoV-1 (Tor2) TSYECDIPIGAGICAS<sup>Y</sup>HTVSL<sup>L</sup>-----R<sup>TS</sup>SQ<sup>S</sup>KSI<sup>I</sup>VAYTMS  
\*\*\*\*\* \*\*

**Fig. S1. SARS-CoV-2 phylogeny and stock generation. (a)** Phylogenetic tree of recent clinical SARS-CoV-2 isolates, with the SARS-CoV-2 strain used in the current study indicated in red. Phylogenetic analysis confirmed a close evolutionary relationship of the isolate BetaCoV/Belgium/GHB-03021/2020 (EPI ISL 407976|2020-02-03) with the prototypic Wuhan-Hu-1 2019-nCoV strain (GenBank accession number MN908947.3). **(b)** Passaging (P) history of the SARS-CoV-2 isolate used indicating the origin and key characteristics of the virus stocks P4 and P6. Two in-frame deletions in the N-terminal domain and the furin-cleavage site of Spike (S) glycoprotein (9aa and 5aa, respectively) were observed in P4 (mixed population of 85% WT genomes and 15% (9+5aa del) mutant genomes). P6 only contains the (9+5aa del) mutant genomes. As a consequence, P4 is an intermediate between the original P0 WT virus and the P6 virus. **(c)** Alignment of parts of the Spike protein of SARS-CoV-2 isolates P0 and P6 with those of the prototypic Wuhan-Hu-1 strain<sup>1,2</sup>, and SARS-CoV-1 (Tor2 strain)<sup>3</sup>. Upper panel – deletion discovered in the N-terminal domain (NTD); lower panel – deletion at the polybasic furin recognition site (shaded box)<sup>4,5</sup>; \* – residue conserved between SARS-CoV-1 and SARS-CoV-2; **BOLD** – predicted O-glycosylation acceptor<sup>6</sup>; S1/S2 – junction between the membrane-distal S1 and membrane-proximal S2 subunits.

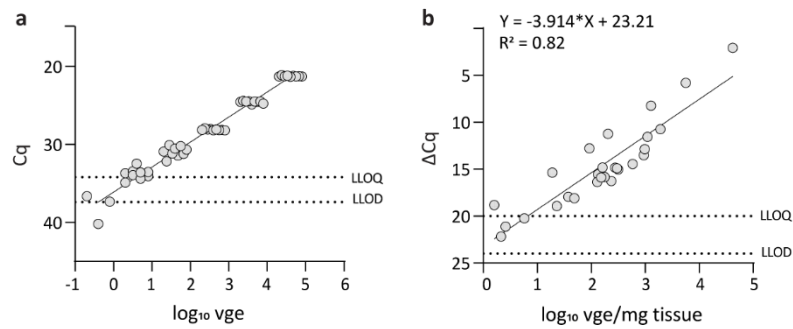
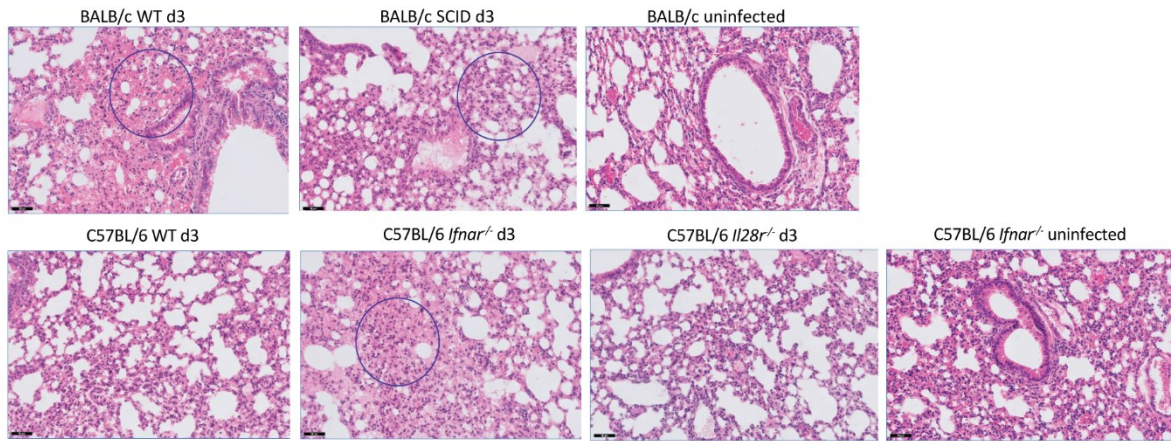


**Fig. S2. Correlation curves for quantification of viral loads in mice. (a)** Correlation between cycle of quantification (Cq) and log<sub>10</sub> viral genome equivalents (vge) obtained from a cDNA plasmid standard. **(b)** Correlation between delta Cq and log<sub>10</sub> vge/mg lung tissue in mice. Delta Cq values are calculated by subtracting Cq values of β-actin from Cq values of SARS-CoV-2. To express viral loads in the lungs of mice, this correlation was used to transform delta Cq values into *Normalized log<sub>10</sub> vge/mg tissue*. Lowest limit of quantification (LLOQ) was defined as lowest detectable value in the linear range of the calibration curve. Lowest limit of detection (LLOD) was defined as lowest detectable value below the linear range of the calibration curve.

**a** Lung pathology H&E scoring



**b** Histopathological scores of H&E images

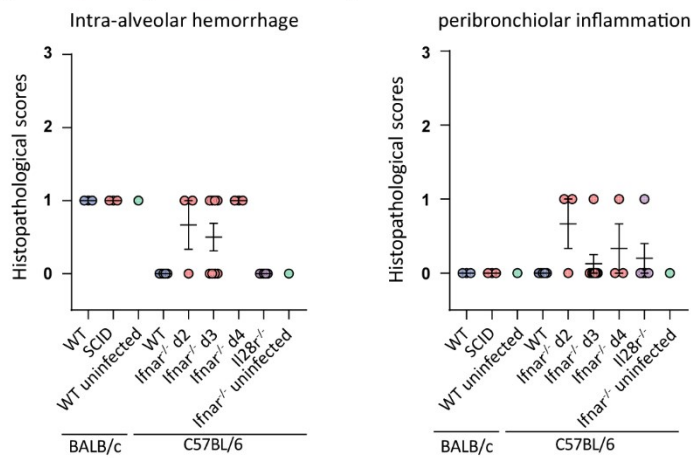


**Fig. S3. Lung pathology in mice.** (a) Representative H&E images of the lungs of uninfected (green circles, n=1) or SARS-CoV-2 infected WT (blue circles, n=3) and SCID (red circles, n=3) BALB/c and WT (blue circles, n=5), *Ifnar1*<sup>-/-</sup> (red circles; day 2 d.p.i. (n=3), day 3 d.p.i. (n=8), day 4 d.p.i. (n=3)) and *Il28r*<sup>-/-</sup> (purple circles, n=5) C57BL/6 mice. Circles indicate presence of intra-alveolar hemorrhage. Black scalebar: 50 μm (b) Histopathological scoring on a scale of 0-3 of intra-alveolar hemorrhage and peribronchiolar inflammation (WT – blue circles; SCID or *Ifnar1*<sup>-/-</sup> – red; *Il28r*<sup>-/-</sup> – purple; uninfected controls – green). The data shown are means ± SEM.

# Hierarchical clustering analysis

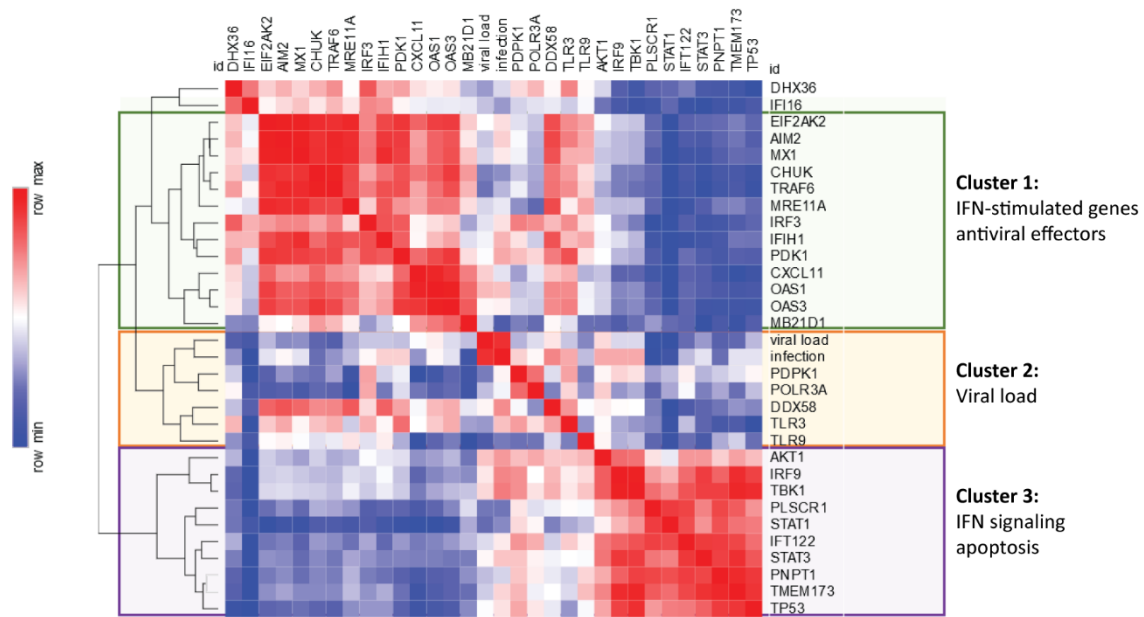


**Fig. S4. Hierarchical clustering analysis of transcriptomic data from uninfected and SARS-CoV-2-infected *Ifnar1*<sup>-/-</sup> mice.** Cluster dendrogram (Euclidean distance) and heatmap of Spearman correlation coefficients between molecular and virological data from uninfected and SARS-CoV-2-infected *Ifnar1*<sup>-/-</sup> mice (n=3 each, analysis on samples of day 3 p.i.), based on a transcriptomic analysis of 30 selected marker genes<sup>7</sup> (Table S2). Hierarchical cluster analysis reveals three main clusters as indicated. A small intermediate cluster (Cluster 2) containing nucleic acid sensors *TLR3/TLR9/DDX58/POLR3A* correlates with viral load. Clusters 1 and 3 are negatively correlated to each other and independent of viral load. Cluster 1 is enriched (p<0.001) for antiviral effector molecules such as *cGAS*, *Mx1*, *IFIH1/MDA-5*, *IRF3*, *OAS1*, *OAS3* and *PKR/EIF2AK2*<sup>8</sup>. Cluster 3 comprises upstream regulators *STAT1*, *STAT3* and *STING/TMEM173* but also *PLSCR1* (scramblase) and *p53*, linking IFN signaling to apoptosis (enrichment p<0.001)<sup>9</sup>. In contrast, *IFI16* decreases upon SARS-CoV-2 infection and clusters independently with *DHX36*, suggesting absence of inflammatory pyroptosis and/or *DHX36*-amplified innate immunity, in line with a fast control of viral replication and limited tissue damage as observed in mice<sup>10</sup>.

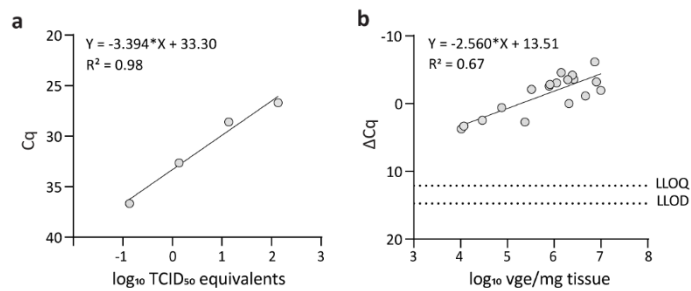


**Fig. S5. Correlation curves for quantification of viral loads in hamsters. (a)** Correlation between cycle of quantification (Cq) and log<sub>10</sub> TCID<sub>50</sub> equivalents obtained from an infectious virus standard. **(b)** Correlation between delta Cq and log<sub>10</sub> vge/mg tissue in hamsters. Delta Cq values are calculated by subtracting Cq values of β-actin from Cq values of SARS-CoV-2. To express viral loads in the different tissue of hamsters, this correlation was used to transform delta Cq values into *Normalized log<sub>10</sub> vge/mg tissue*. Lowest limit of quantification (LLOQ) was defined as lowest detectable value in the linear range of the calibration curve. Lowest limit of detection (LLOD) was defined as lowest detectable value below the linear range of the calibration curve.

Viral RNA in human Calu-3 cells

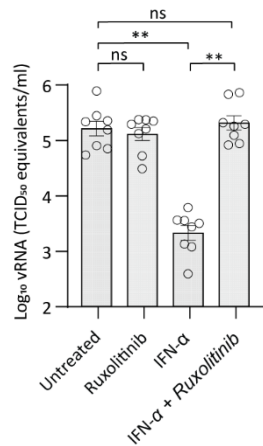


**Fig. S6.** Inhibition of JAK/STAT signaling by Ruxolitinib can rescue SARS-CoV-2 virus replication from the antiviral effect of Type-I IFN. Calu-3 cells<sup>11</sup> were left untreated or treated with Ruxolitinib (4  $\mu$ M), IFN- $\alpha$  (10 IU/mL) or a combination of both (n=8 for each condition). Treatment was initiated 4 h before infection and was continued through the whole experiment. Cultures were infected with P4 SARS-CoV-2 (MOI of 0.1), 48 h p.i. cell culture SN was collected, RNA was extracted and vRNA levels were quantified using RT-qPCR. The data shown are means  $\pm$  SEM. Statistical significance between groups was calculated by Kruskal-Wallis with a two-sided Dunn's post hoc test. P values: \*\*P = 0.0035 and \*\*P=0.0019 (left to right); ns, not significant.



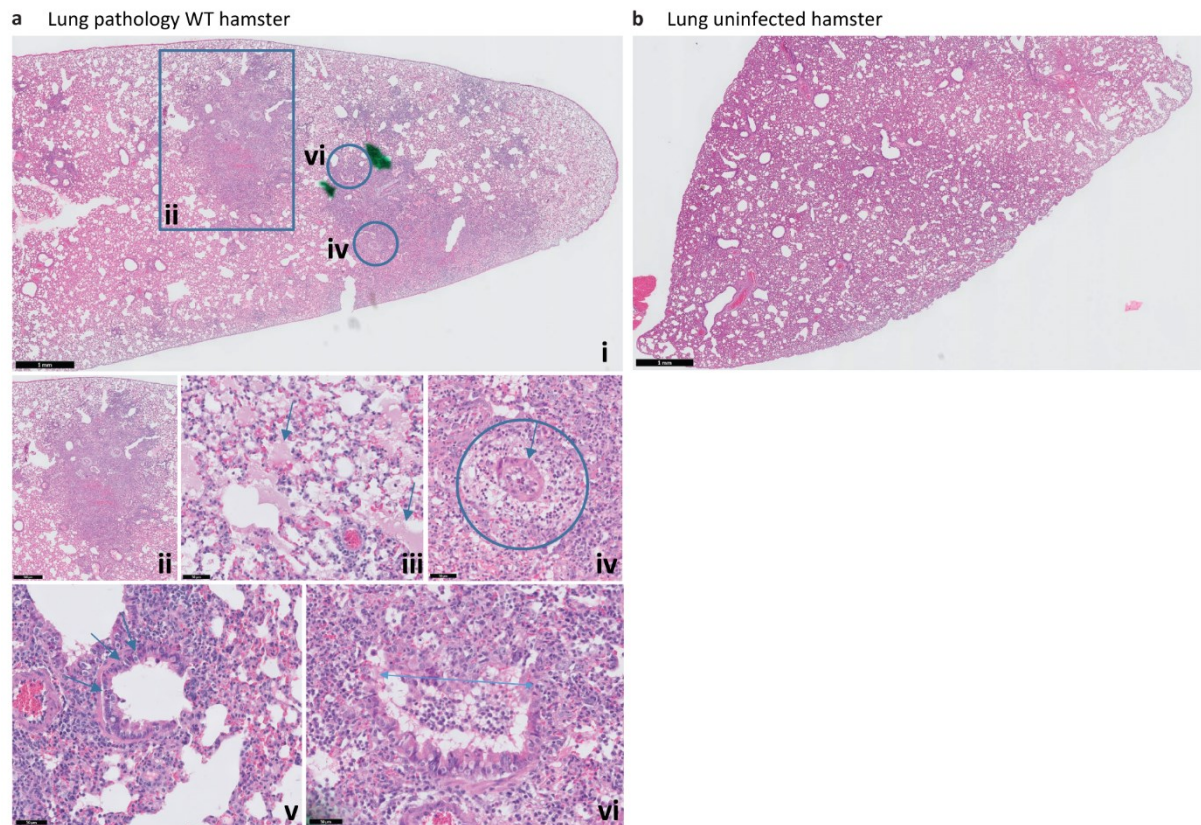


**Fig. S7. Lung pathology in a WT hamster.** **(a)** Representative H&E images of the lung of a SARS-CoV-2 infected WT hamster. **(Panel i)** rectangle bronchopneumonia (see also panel b), upper circle necrotizing bronchiolitis (see also panel f), lower circle perivascular edema (see also panel d) (black scalebar: 1mm). **(Panel ii)** area of bronchopneumonia with inflammation centered around a bronchus (magnification of panel a) (black scalebar: 0.5mm). **(Panel iii)** intra-alveolar hemorrhage and edema (arrows) (black scalebar: 50 $\mu$ m). **(Panel iv)** perivascular edema (circle), vascular wall (arrow) is surrounded by loose fibrous tissue and a few inflammatory cells (magnification of panel a) (black scalebar: 50 $\mu$ m). **(Panel v)** bronchus with apoptotic cells (arrows) (black scalebar: 50 $\mu$ m). **(Panel vi)** necrotizing bronchiolitis: half of the bronchus wall has disappeared and is replaced by inflammatory cells (arrow, magnification of panel a) (black scalebar: 50 $\mu$ m). **(b)** Representative H&E image of the lung of an uninfected WT hamster (black scalebar: 1mm). The images in **a** are representative images from two independent experiments (n=7 animals); the image in **b** is from one experiment (n=1 animal)

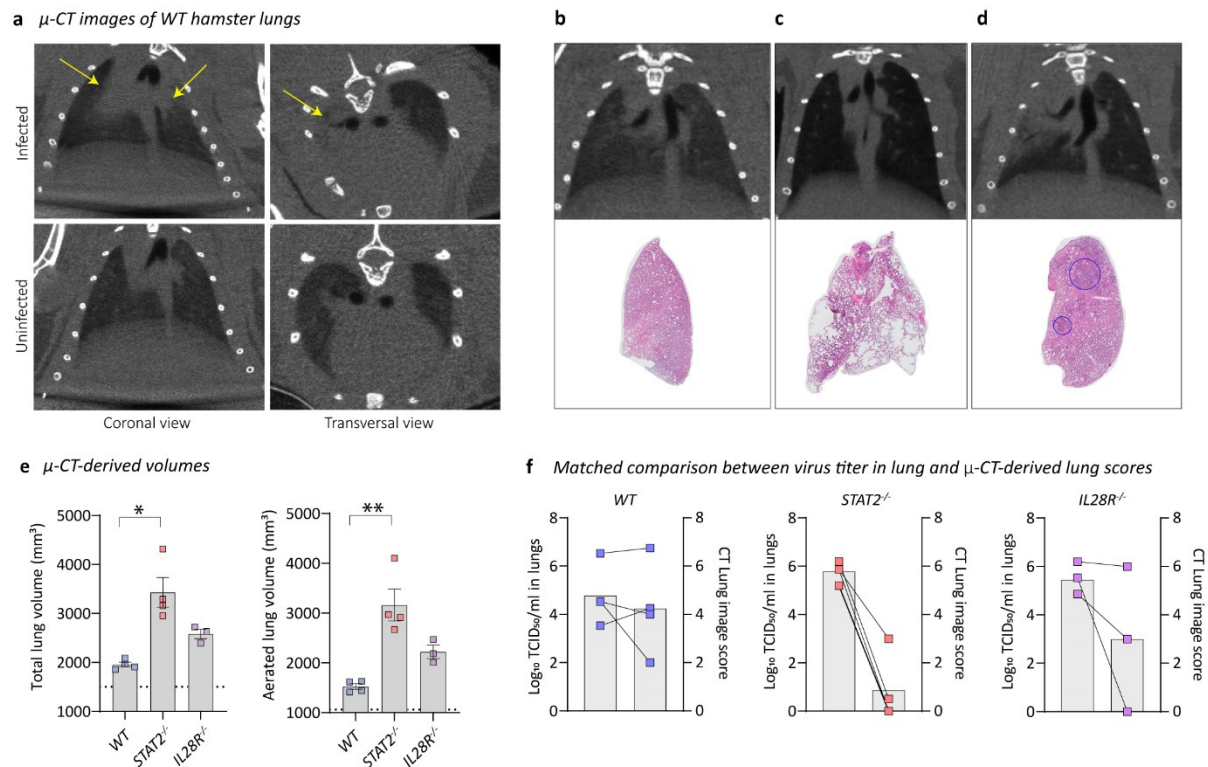
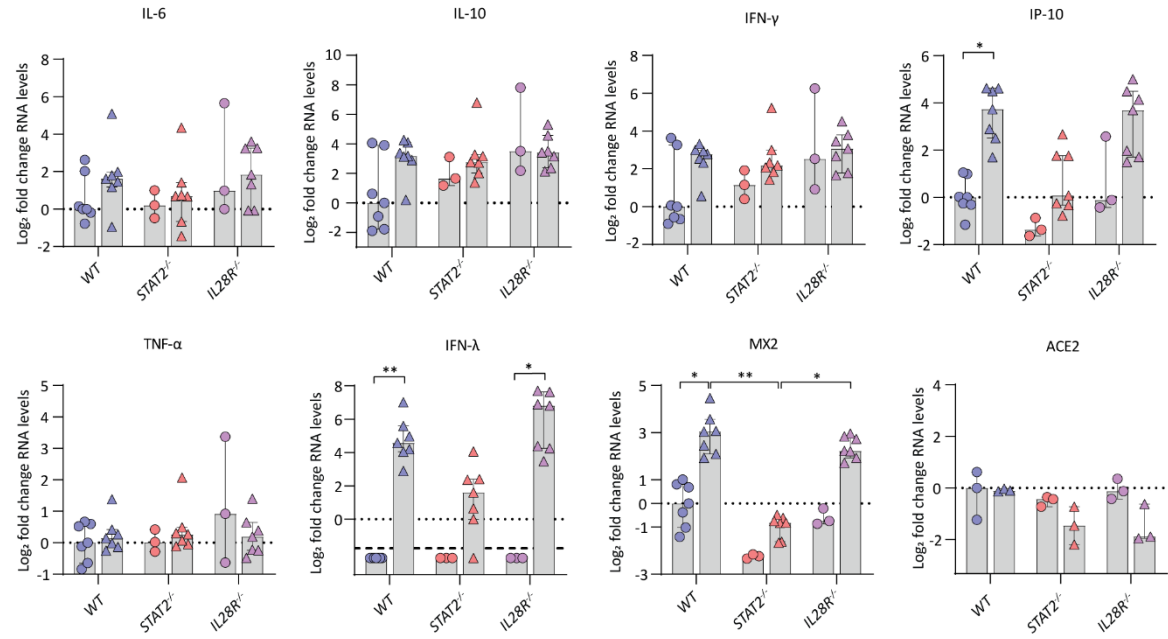


**Fig. S8. Micro-CT-observed lung pathology.** (a) Representative coronal and transversal micro-CT ( $\mu$ CT) images of an upper airway enlargement and dense lung infiltrates in the lungs of infected (P6 SARS-CoV-2) WT hamsters compared to uninfected hamsters. Yellow arrows indicate examples of pulmonary infiltrates seen as consolidation of lung parenchyma. (b) Coronal micro-CT image (left top) and histopathological H&E-stained section of whole lobe (left bottom) and of a healthy, uninfected hamster lung. (c) Histopathology confirmed hyperinflation visualized on the micro-CT scan as decreased density (blackening) of lung tissue and overall lung enlargement, seen in one infected *STAT2*<sup>-/-</sup> hamster. (d) Consolidation of right lung parenchyma on micro-CT corresponds to bronchopneumonia evidenced by histopathology (darker blue stained areas, blue circles) of an infected *IL28R*<sup>-/-</sup> hamster. (e) Micro-CT-derived biomarkers quantifying total lung volume and aerated lung volume (see also Fig. 3e) of infected WT (blue squares, n=4), *STAT2*<sup>-/-</sup> (red squares, n=4) and *IL28R*<sup>-/-</sup> (purple squares, n=3) hamsters. Lines indicate micro-CT-derived biomarkers in healthy animals (n=3). The data shown are means  $\pm$  SEM. (f) Matched comparison between infectious viral load in the lung (left Y-axis) (values from Fig. 2c) and  $\mu$ CT-derived semi-quantitative lung scores (values from Fig. 3d) (right Y-axis) (n=4 for WT and *STAT2*<sup>-/-</sup> and n=3 for *IL28R*<sup>-/-</sup>). Lines indicate matched samples. Statistical significance between genotypes was calculated by the Kruskal-Wallis with a two-sided Dunn's post hoc test. P values: \*P=0.043 and \*P=0.0030 (left to right in e).



**a Gene expression in lung**



**b Spearman Correlations**

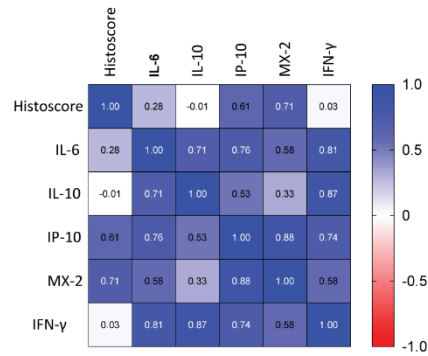


**Fig. S9. RNA expression levels after SARS-CoV-2 infection. (a)** Individual expression profiles for IL-6, IL-10, IFN-γ, IP-10, TNF-α, IFN-λ, MX2 and ACE2 in lungs of WT (blue), *STAT2*<sup>-/-</sup> (red) and *IL28R*<sup>-/-</sup> (purple) hamsters four days after SARS-CoV-2 infection (n=7 for each genotype) (as in Figure 3f and g) presented as log<sub>2</sub>-fold change relative to uninfected WT controls (blue circles, n=7). Levels of individual mRNAs in uninfected (circles) and infected (triangles) animals were determined by RT-qPCR and normalized for β-actin mRNA. Changes are reported as values over the median of uninfected controls (dotted line) calculated using the  $2^{(-\Delta\Delta Cq)}$  method. Only for IFN-λ, where control animals had undetectable mRNA levels, values were compared to the lowest detectable value (dashed line). Data presented as median ± IQR. **(b)** Heatmap of Spearman correlation coefficients between normalized gene expression levels (Fig. 3f and panel a of this figure) and histology data (derived from Fig. 3a) from uninfected and SARS-CoV-2-infected hamsters. Positive correlations were used in Fig. 3h to show a correlation between increased lung pathology and increased gene expression in the different genotypes. Statistical significance between groups was calculated by Kruskal-Wallis with a two-sided Dunn's post hoc test. P values: \*P=0.012 (top a); \*\*P=0.0061, \*P=0.026, \*P=0.039, \*\*P=0.0014 and \*P=0.012 (bottom left to right a).

**Supplementary Table S1.** Primers and probes used for RT-qPCR

Gene	Description	Oligonucleotide sequence
<b>SARS-CoV-2</b>	Primer 1	5'-TTA CAA ACA TTG GCC GCA AA-3'
	Primer 2	5'-GCG CGA CAT TCC GAA GAA-3'
	Probe	5'-FAM-ACA ATT TGC CCC CAG CGC TTC AG-BHQ1-3'
<b>Mouse <i>Actb</i></b>	Primer 1	5'-GAT TAC TGC TCT GGC TCC TAG-3'
	Primer 2	5'-GAC TCA TCG TAC TCC TGC TTG-3'
	Probe	5'-FAM-CTG GCC TCA CTG TCC ACC TTC C-ZEN/IABkFQ-3'
<b>Hamster <i>ACE2</i></b>	Primer 1	5'-GGG AAC TGT CAA AGG GTA CAG-3'
	Primer 2	5'-CCC TTC CTA CAT CAG TCC TAC T-3'
	Probe	5'-FAM-TCC CTG CTC ATT TGC TTG GTG ACA-ZEN/IABkFQ-3'
<b>Hamster <i>ACTB</i></b>	Primer 1	5'-GGC CAG GTC ATC ACC ATT-3'
	Primer 2	5'-GAG TTG AAT GTA GTT TCG TGG ATG-3'
	Probe	5'-Cy5-TTT CCA GCC TTC CTT CCT GGG TAT G-IBRQ-3'
<b>Hamster <i>IFN-γ</i></b>	Primer 1	5'-TTT CTC CAT GCT GCT GTT GAA-3'
	Primer 2	5'-GGC CAT CCA GAG GAG CAT AG-3'
	Probe	5'-FAM-CAC CAT CAA GGC AGA CCT GTT TGC TAA CTT-ZEN/IABkFQ-3'
<b>Hamster <i>IFNλ</i></b>	Primer 1	5'-CCC ACC AGA TGC AAA GGA TT-3'
	Primer 2	5'-CTT GAG CAG CCA CTC TTC TAT G-3'
	Probe	5'-FAM-ACA TAG CCC GGT TCA AGT CTC TGC-ZEN/IABkFQ-3'
<b>Hamster <i>IL-6</i></b>	Primer 1	5'-GGT ATG CTA AGG CAC AGC ACA CT-3'
	Primer 2	5'-CCT GAA AGC ACT TGA AGA ATT CC-3'
	Probe	5'-FAM-AGA AGT CAC CAT GAG GTC TAC TCG GCA AAA-ZEN/IABkFQ-3'
<b>Hamster <i>IL-10</i></b>	Primer 1	5'-TTC TGG CCC GTG GTT CTC T-3'
	Primer 2	5'-GTT GCC AAA CCT TAT CAG AAA TGA-3'
	Probe	5'-FAM-CAG TTT TAC CTG GTA GAA GTG ATG CCC CAG G-ZEN/IABkFQ-3'
<b>Hamster <i>IP-10</i></b>	Primer 1	5'-GCC ATT CAT CCA CAG TTG ACA-3'
	Primer 2	5'-CAT GGT GCT GAC AGT GGA GTC T-3'
	Probe	5'-FAM-CGT CCC GAG CCA GCC AAC GA-ZEN/IABkFQ-3'
<b>Hamster <i>MX2</i></b>	Primer 1	5'-CCA GTA ATG TGG ACA TTG CC-3'
	Primer 2	5'-CAT CAA CGA CCT TGT CTT CAG TA-3'
	Probe	5'-FAM-TGT CCA CCA GAT CAG GCT TGG TCA-ZEN/IABkFQ-3'
<b>Hamster <i>TNF-α</i></b>	Primer 1	5'-AGC TGG TTG TCT TTG AGA GAC ATG-3'
	Primer 2	5'-GGA GTG GCT GAG CCA TCG T-3'
	Probe	5'-FAM-CCA ATG CCC TCC TGG CCA ACG-ZEN/IABkFQ-3'

**Supplementary Table S2.** RT-qPCR Taqman assays for analysis of DEG in SARS-CoV-2 infected cells

Gene of Interest	Proposed MoA in immune response	Reference	Assay ID
<i>18s rRNA</i>	House keeping gene		<a href="#">Hs99999901_s1</a>
<i>GAPDH</i>	House keeping gene		<a href="#">Mm99999915_g1</a>
<i>AIM2</i>	Cytosolic DNA sensor	Yu and Levine <sup>12</sup>	<a href="#">Mm01295719_m1</a>
<i>AKT1</i>	Controls innate immune cell development and function	Zhang et al <sup>13</sup>	<a href="#">Mm01331626_m1</a>
<i>CHUK (IKK)</i>	Inhibitor of nuclear factor kappa-B kinase subunit alpha (IKK- $\alpha$ )	Llona-Minguez et al <sup>14</sup>	<a href="#">Mm00432529_m1</a>
<i>CXCL11</i>	Interferon inducible T cell alpha chemoattractant	Venter et al <sup>15</sup>	<a href="#">Mm00444662_m1</a>
<i>DHX36</i>	Enhances RIG-I Signaling	Yoo et al <sup>16</sup>	<a href="#">Mm00661002_m1</a>
<i>DDX58</i>	Antiviral, IFN signalling, innate immune receptor	Pulendran et al <sup>17</sup> , Querec et al <sup>18</sup>	<a href="#">Mm01216853_m1</a>
<i>EIF2AK 2</i>	Antiviral, IFN signalling	Querec et al <sup>18</sup> , Gaucher et al <sup>19</sup>	<a href="#">Mm01235643_m1</a>
<i>IFI16</i>	Interferon Gamma Inducible Protein 16	Trapani et al <sup>20</sup>	<a href="#">Mm00492602_m1</a>
<i>IFIH1</i>	Antiviral, IFN signalling, innate immune receptor	Pulendran et al <sup>21</sup> , Querec et al <sup>22</sup>	<a href="#">Mm00459183_m1</a>
<i>IFT122</i>	Intraflagellar Transport 122	Boubakri et al <sup>23</sup>	<a href="#">Mm00661643_m1</a>
<i>IRF3</i>	Interferon regulatory factor 3	Collins et al <sup>24</sup>	<a href="#">Mm00516784_m1</a>
<i>IRF9</i>	Antiviral, IFN signalling	Gaucher et al <sup>19</sup>	<a href="#">Mm00492679_m1</a>
<i>MB21D1(cGAS)</i>	Cytosolic DNA sensor	Liang et al <sup>25</sup>	<a href="#">Mm01147496_m1</a>
<i>MRE11</i>	Double strand break repair nuclease	Shibata et al <sup>26</sup>	<a href="#">Mm00450600_m1</a>
<i>OAS1</i>	Antiviral, IFN signalling	Gaucher et al <sup>19</sup>	<a href="#">Mm00449297_m1</a>
<i>OAS3</i>	Antiviral, IFN signalling	Gaucher et al <sup>19</sup>	<a href="#">Mm00460944_m1</a>
<i>MX1</i>	Antiviral, IFN signalling	Querec et al <sup>18</sup> , Gaucher et al <sup>19</sup>	<a href="#">Mm00487796_m1</a>
<i>PDK1</i>	Key role in regulation of glucose and fatty acid metabolism	Tan et al <sup>27</sup>	<a href="#">Mm00554300_m1</a>
<i>PDPK1</i>	Important role in the signalling pathways	Sato et al <sup>28</sup>	<a href="#">Mm00440707_m1</a>
<i>PLSCR1</i>	Antiviral, IFN signalling	Querec et al <sup>18</sup> , Gaucher et al <sup>19</sup>	<a href="#">Mm01228223_g1</a>
<i>PNPT1</i>	Antiviral, IFN signalling, innate immune receptor	Pulendran et al <sup>21</sup> , Querec et al <sup>18</sup>	<a href="#">Mm00466286_m1</a>

<i>STAT1</i>	Key regulators of the early innate immune response	Decker et al <sup>29</sup>	<a href="#">Mm01257286_m1</a>
<i>STAT3</i>	Control of inflammation and immunity	Hillmer et al <sup>30</sup>	<a href="#">Mm01219775_m1</a>
<i>TBK1</i>	Protein kinase downstream of TMEM173 (STING)	Lam et al <sup>31</sup>	<a href="#">Mm00451150_m1</a>
<i>TLR3</i>	pattern-recognition receptors (PRRs)	Yu and Levine <sup>12</sup>	<a href="#">Mm01207404_m1</a>
<i>TLR9</i>	Cytosolic DNA sensor	Yu and Levine <sup>12</sup>	<a href="#">Mm07299609_m1</a>
<i>TMEM173(STING)</i>	Stimulator of IFN response	Lam et al <sup>31</sup>	<a href="#">Mm01158117_m1</a>
<i>TP53</i>	Tumor protein 53	Matlashewski et al <sup>32</sup>	<a href="#">Mm00480750_m1</a>
<i>TRAF6</i>	TNF receptor associated factor (TRAF)	Youseff et al <sup>33</sup>	<a href="#">Mm00493836_m1</a>

## References to Supplementary Material

1. Wrapp, D. *et al.* Cryo-EM structure of the 2019-nCoV spike in the prefusion conformation. *Science* (80-. ). **367**, 1260–1263 (2020).
2. Wu, F. *et al.* A new coronavirus associated with human respiratory disease in China. *Nature* **579**, 265–269 (2020).
3. Marra, M. A. *et al.* The genome sequence of the SARS-associated coronavirus. *Science* (80-. ). **300**, 1399–1404 (2003).
4. Zhang, T., Wu, Q. & Zhang, Z. Probable Pangolin Origin of SARS-CoV-2 Associated with the COVID-19 Outbreak. *Curr. Biol.* **30**, 1346-1351.e2 (2020).
5. Zhang, Y.-Z. & Holmes, E. C. A Genomic Perspective on the Origin and Emergence of SARS-CoV-2. *Cell* (2020) doi:10.1016/j.cell.2020.03.035.
6. Andersen, K. G., Rambaut, A., Lipkin, W. I., Holmes, E. C. & Garry, R. F. The proximal origin of SARS-CoV-2. *Nat. Med.* **26**, 450–452 (2020).
7. Sharma, S. *et al.* Small molecule inhibitors of TBK1 serve as adjuvant for a plasmid-launched live-attenuated yellow fever vaccine. *Hum. Vaccines Immunother.* (2020).
8. Schoggins, J. W. Interferon-Stimulated Genes: What Do They All Do? *Annu. Rev. Virol.* **6**, 567–584 (2019).
9. Khouri, R. *et al.* A genetic IFN/STAT1/FAS axis determines CD4 T stem cell memory levels and apoptosis in healthy controls and Adult T-cell Leukemia patients. *Oncoimmunology* **7**, (2018).
10. Briard, B., Place, D. E. & Kanneganti, T. D. DNA sensing in the innate immune response. *Physiology* vol. 35 112–124 (2020).
11. Hoffmann, M. *et al.* SARS-CoV-2 Cell Entry Depends on ACE2 and TMPRSS2 and Is Blocked by a Clinically Proven Protease Inhibitor. *Cell* **181**, 271-280.e8 (2020).
12. Yu, M. & Levine, S. J. Toll-like receptor 3, RIG-I-like receptors and the NLRP3 inflammasome: Key modulators of innate immune responses to double-stranded RNA viruses. *Cytokine and Growth Factor Reviews* vol. 22 63–72 (2011).
13. Zhang, Y. *et al.* Kinase AKT controls innate immune cell development and function. *Immunology* **140**, 143–152 (2013).
14. Llona-Minguez, S., Baiget, J. & Mackay, S. P. Small-molecule inhibitors of I $\kappa$ B kinase (IKK) and IKK-related kinases. *Pharm. Pat. Anal.* **2**, 481–498 (2013).
15. Venter, M. *et al.* Gene expression in mice infected with West Nile virus strains of different neurovirulence. *Virology* **342**, 119–140 (2005).
16. Yoo, J. S. *et al.* DHX36 Enhances RIG-I Signaling by Facilitating PKR-Mediated Antiviral Stress Granule Formation. *PLoS Pathog.* **10**, (2014).
17. Pulendran, B. Learning immunology from the yellow fever vaccine: Innate immunity to systems vaccinology. *Nature Reviews Immunology* vol. 9 741–747 (2009).
18. Querec, T., Akondy, R., Lee, E., ... W. C.-N. & 2009, undefined. Systems biology approach predicts immunogenicity of the yellow fever vaccine in humans. *nature.com*.
19. Gaucher, D. *et al.* Yellow fever vaccine induces integrated multilineage and polyfunctional immune responses. *J. Exp. Med.* (2008) doi:10.1084/jem.20082292.

20. Trapani, J. A., Dawson, M., Apostolidis, V. A. & Browne, K. A. Genomic organization of IFI16, an interferon-inducible gene whose expression is associated with human myeloid cell differentiation: correlation of predicted protein domains with exon organization. *Immunogenetics* **40**, 415–424 (1994).
21. Pulendran, B. Learning immunology from the yellow fever vaccine: Innate immunity to systems vaccinology. *Nature Reviews Immunology* vol. 9 741–747 (2009).
22. Querec, T. D. *et al.* Systems biology approach predicts immunogenicity of the yellow fever vaccine in humans. *Nat. Immunol.* **10**, 116–125 (2009).
23. Boubakri, M. *et al.* Loss of ift122, a Retrograde Intraflagellar Transport (IFT) complex component, leads to slow, progressive photoreceptor degeneration due to inefficient opsin transport. *J. Biol. Chem.* **291**, 24465–24474 (2016).
24. Collins, S. E., Noyce, R. S. & Mossman, K. L. Innate Cellular Response to Virus Particle Entry Requires IRF3 but Not Virus Replication. *J. Virol.* **78**, 1706–1717 (2004).
25. Liang, Y. & Peng, H. STING-cytosolic DNA sensing: The backbone for an effective tumor radiation therapy. *Annals of Translational Medicine* vol. 4 (2016).
26. Shibata, A. *et al.* DNA Double-Strand Break Repair Pathway Choice Is Directed by Distinct MRE11 Nuclease Activities. *Mol. Cell* **53**, 7–18 (2014).
27. Tan, J. *et al.* PDK1 signaling toward PLK1-MYC activation confers oncogenic transformation, tumor-initiating cell activation, and resistance to mTOR-targeted therapy. *Cancer Discov.* **3**, 1156–1171 (2013).
28. Sato, S., Fujita, N. & Tsuruo, T. Regulation of kinase activity of 3-phosphoinositide-dependent protein kinase-1 by binding to 14-3-3. *J. Biol. Chem.* **277**, 39360–39367 (2002).
29. Decker, T., Stockinger, S., Karaghiosoff, M., Müller, M. & Kovarik, P. IFNs and STATs in innate immunity to microorganisms. *J. Clin. Invest.* **109**, 1271–1277 (2002).
30. Hillmer, E. J., Zhang, H., Li, H. S. & Watowich, S. S. STAT3 signaling in immunity. *Cytokine and Growth Factor Reviews* vol. 31 1–15 (2016).
31. Lam, E., Stein, S. & Falck-Pedersen, E. Adenovirus Detection by the cGAS/STING/TBK1 DNA Sensing Cascade. *J. Virol.* **88**, 974–981 (2014).
32. Matlashewski, G. *et al.* Isolation and characterization of a human p53 cDNA clone: expression of the human p53 gene. *EMBO J.* **3**, 3257–3262 (1984).
33. Youseff, B. H. *et al.* TRAF6 Plays a Proviral Role in Tick-Borne Flavivirus Infection through Interaction with the NS3 Protease. *iScience* **15**, 489–501 (2019).